Nano Research 2015, 8(3): 967–979
DOI 10.1007/s12274-014-0578-9
Research Article

ISSN 1998-0124
CN 11-5974/O4

Topological crystalline insulator nanomembrane with strain-tunable band gap

Xiaofeng Qian[1], Liang Fu[2] (✉), and Ju Li[1] (✉)

[1] *Department of Nuclear Science and Engineering and Department of Materials Science and Engineering, Massachusetts Institute of Technology, Cambridge, Massachusetts 02139, USA*
[2] *Department of Physics, Massachusetts Institute of Technology, Cambridge, Massachusetts 02139, USA*

Received: 10 May 2013
Revised: 31 August 2014
Accepted: 6 September 2014

© Tsinghua University Press and Springer-Verlag Berlin Heidelberg 2014

KEYWORDS

elastic strain engineering, pseudoheterostructure, infrared photodetector, metal–insulator transition, DFT calculations

ABSTRACT

The ability to fine-tune band gap and band inversion in topological materials is highly desirable for the development of novel functional devices. Here we propose that the electronic properties of free-standing nanomembranes of the topological crystalline insulators (TCI) SnTe and $Pb_{1-x}Sn_x$(Se,Te) are highly tunable by engineering elastic strain and membrane thickness, resulting in tunable band gap and giant piezoconductivity. Membrane thickness governs the hybridization of topological electronic states on opposite surfaces, while elastic strain can further modulate the hybridization strength by controlling the penetration length of surface states. We propose a frequency-resolved infrared photodetector using force-concentration induced inhomogeneous elastic strain in TCI nanomembranes with spatially varying width. The predicted tunable band gap accompanied by strong spin-textured electronic states will open new avenues for fabricating piezoresistive devices, infrared detectors and energy-efficient electronic and spintronic devices based on TCI nanomembrane.

1 Introduction

The ability to tune band gap and control band inversion in topological materials [1, 2] is desirable for the development of novel functional devices. Such band gap engineering has been demonstrated for Bi-based topological insulators using various methods such as alloying [3, 4], thickness engineering [5–7] and magnetic proximity effects [8–11]. A useful and potentially advantageous alternative approach is elastic strain engineering [12, 13]. While there have been extensive theoretical studies of strain-tunable band gaps in topological insulators [13–22], to our knowledge a device utilizing this effect has not yet been demonstrated.

The recently discovered topological crystalline insulators (TCI) [23, 24] in IV–VI semiconductors SnTe [25] and $Pb_{1-x}Sn_x$Se(Te) [26–28] provide a new platform for topological band gap engineering via elastic strain. In this work, by first-principles calculations we demonstrate a new approach to effective band gap engineering by controlling elastic strain and

Address correspondence to Liang Fu, liangfu@mit.edu; Ju Li, liju@mit.edu

membrane thickness in TCI membranes, which is based on the unique electronic properties of TCI surface states. Specifically, we find that strain induces a wave vector (***k***) shift of surface-state Dirac cones and thereby continuously changes the penetration depth of surface states. In a free-standing TCI membrane with two surfaces, the above will cause an exponential change in the hopping integral between the top and bottom surface states and thus drastically modulate the hybridization gap from 0 to 0.5 eV. This thickness- and elastic strain-dependent two-dimensional band gap leads to potential applications in piezoresistive devices, tunable infrared detectors, and thermoelectrics. In particular, we propose a frequency-resolved infrared photodetector using force–concentration induced inhomogeneous elastic strain in TCI nanomembranes.

Our main results are applicable to TCIs in the IV–VI semiconductor family, and we choose SnTe as a representative material. As shown later, the electronic structure change in SnTe nanomembranes under elastic strain is a direct consequence of the corresponding change in the infinite and the semi-infinite SnTe, and therefore our calculations and analyses will address three progressively more complex geometries: (a) infinite bulk with 3D band structure, (b) semi-infinite bulk with a single free surface and 2D surface band structure, and (c) nanomembrane with two coupled surfaces and 2D band structure.

2 Electronic structure in SnTe

2.1 Bulk SnTe

The fundamental band gap of bulk SnTe is located at the L points of the 3D Brillouin zone (BZ). Most importantly, there exists band inversion at these *R*(*L*) points under strain-free conditions, i.e., the anions dominate the lowest conduction band while the cations dominate the highest valence band, which is a necessary condition for realizing the TCI phase and creating localization-resistant topological surface states [24]. Using first-principles density-functional theory (DFT) calculations [29, 30], we calculated the bulk band structure of SnTe near *R*(*L*) as a function of in-plane (*x*–*y*) biaxial strain with atomic structure fully relaxed along *z*. The calculated 3D band structure is shown in Fig. 1(e) whose first BZ (purple tetragonal cell) and atomic configuration are shown in Figs. 1(a) and 1(b),

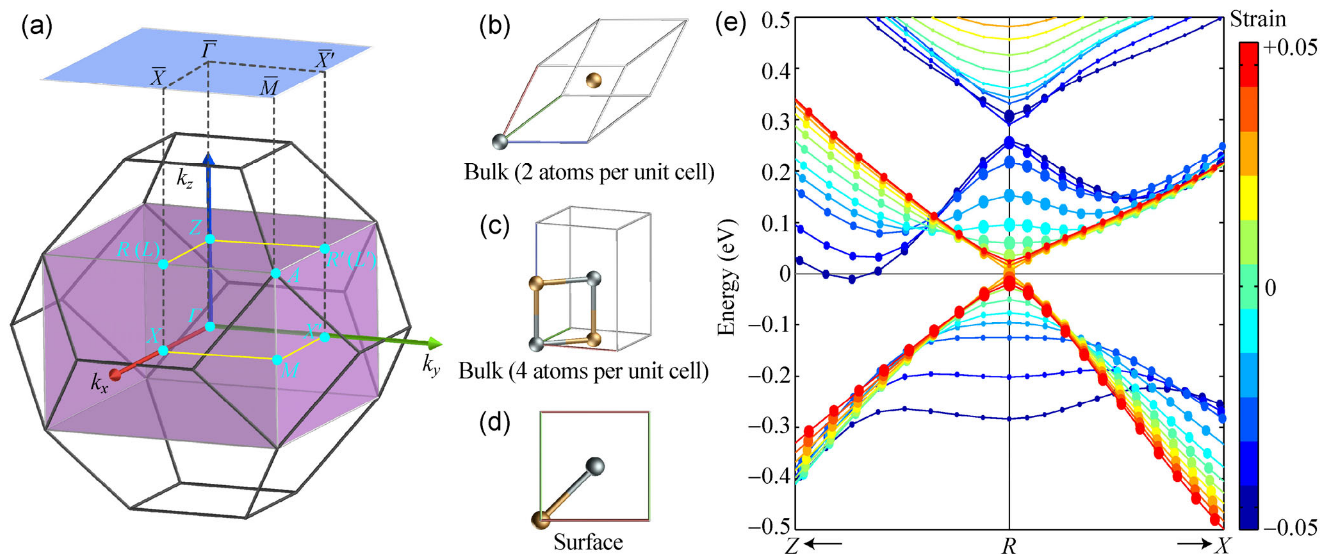

Figure 1 Real and reciprocal space structures of SnTe bulk and membrane in different unit cells, and strain-dependent electronic band structure of bulk SnTe. (a) Brillouin zones for bulk and SnTe membrane in different unit cells. In black is the Brillouin zone for bulk SnTe with two atoms per unit cell with its unit cell shown in (b). In purple one is the Brillouin zone for bulk SnTe with four atoms per unit cell with its unit cell shown in (c). The 2D Brillouin zone in blue is for both a SnTe semi-infinite surface and a SnTe nanomembrane with its top view shown in (d). Sn: gray atoms; Te: yellow atoms. (e) Strain-dependent electronic band structure of bulk SnTe. The dot size indicates the strength of contribution of Te to the density of states.

respectively. The size of the dots in Fig. 1(e) indicates the contribution of Te s and p orbitals to the corresponding electronic state. As the strain increases, the band gap initially decreases, and then opens up again. Above 3% strain, band inversion disappears, that is, Te p orbitals have shifted from the conduction band edge to the valence band edge. Such strain-tunable band inversion and band gap in bulk SnTe provide the basis for a strain-tunable band gap of a 2D SnTe membrane to be described below.

2.2 Semi-infinite SnTe

In order to address the strain- and thickness-dependent band gap in TCI membranes, it is necessary to first characterize the metallic TCI surface state in the semi-infinite limit, where we study the low-energy electronic structure of a single isolated surface. The tight-binding Hamiltonian of a semi-infinite SnTe surface is constructed in the first-principles quasiatomic Wannier function basis [31–33] by knitting the bulk SnTe Hamiltonian and surface Hamiltonian. The latter was cut from a fully relaxed 24-layer SnTe slab. A self-energy correction was further applied to the bulk Hamiltonian by a half-surface Green's function using a highly convergent algorithm [34, 35] often adopted in quantum transport calculations [36]. In Fig. 1(a), symbols with bar on top ($\bar{\Gamma}$, $\bar{X}'$, $\bar{X}$, $\bar{M}$) denote surface Brillouin zone **k**-points. The calculated band structure along $\overline{\Gamma X}$ for a top surface (+z) is shown in Fig. 2(a) with surface BZ shown in Fig. 1(a) (blue square). Two chiral Dirac cones with the same chirality emerge at (E, k_x, k_y) of (E_F, 0.66 Å^{-1}, 0) and (E_F, 0.73 Å^{-1}, 0), respectively. In the vicinity of the cone almost all the spin moment comes from $\langle S\rangle_y$ with its direction marked in Fig. 2(a): red for positive $\langle S\rangle_y$ and blue for negative $\langle S\rangle_y$. The estimated Fermi velocity at the left Dirac cone is 2.8×10^5 m/s for the red band and 1.6×10^5 m/s for the blue band. The asymmetric Fermi velocity results from different dominating components in two bands, that is, the Sn-dominated red band and Te-dominated blue band at the left Dirac cone. In addition, energy contours and spin texture of surface states at the conduction band minimum (CBM), CBM+1, valence band maximum (VBM), and VBM–1 in the 2D BZ are presented in Figs. 2(b)–2(e), revealing a clear anisotropy of both the shape of the Dirac cones and the strength of the spin moment $\langle S\rangle$ in the k_x and k_y directions.

To further reveal the spatial profile and atomic orbital composition of surface states, we present in Fig. 3 the atom-projected local density of states (LDOS) of ten selected surface states near the left Dirac cone

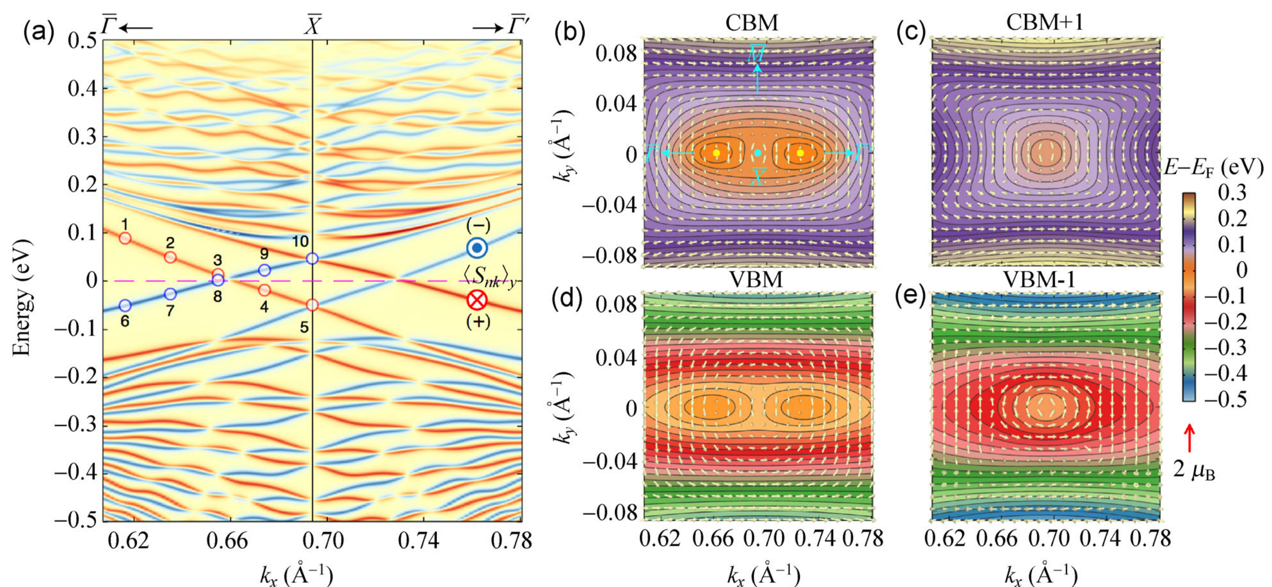

Figure 2 Band structure and spin texture of strain-free semi-infinite SnTe. (a) Band structure of strain-free semi-infinite SnTe color-encoded by spin component along y. Vacuum is in the +z direction. Energy contour and spin texture of surface states at (b) CBM, (c) CBM+1, (d) VBM, and (e) VBM–1 in the 2D Brillouin zone.

with their energy-momentum marked in Fig. 2(a). In order to extract the decay constant, we fit the layer-averaged LDOS to an exponential form, i.e., $\rho_{nk}(z) = c \cdot \exp\left(-|z-z_0|/\lambda_{nk}\right)$, where z_0 denotes the position of the top surface layer in the z direction and λ_{nk} is the decay constant for state n at the $\boldsymbol{k}$-point. The estimated band and $\boldsymbol{k}$-point dependent decay constants λ_{nk} are listed in Fig. 3. The decay length increases as the 2D BZ $\boldsymbol{k}$-point moves towards $\overline{X}$. This is because the $\overline{X}$-point of the 2D BZ contains a projection of the $R(L)$-point in the 3D BZ; as the surface state $\boldsymbol{k}$-point in 2D BZ approaches $\overline{X}$, it comes into energy resonance with bulk band state and is then no longer localized in z. The penetration depth and the amplitude of the atom-projected LDOS also highly depend on the specific type and site of atoms. These characters are also an unambiguous manifestation of band inversion, i.e., VBM and CBM of bulk SnTe are dominated by Sn and Te, respectively.

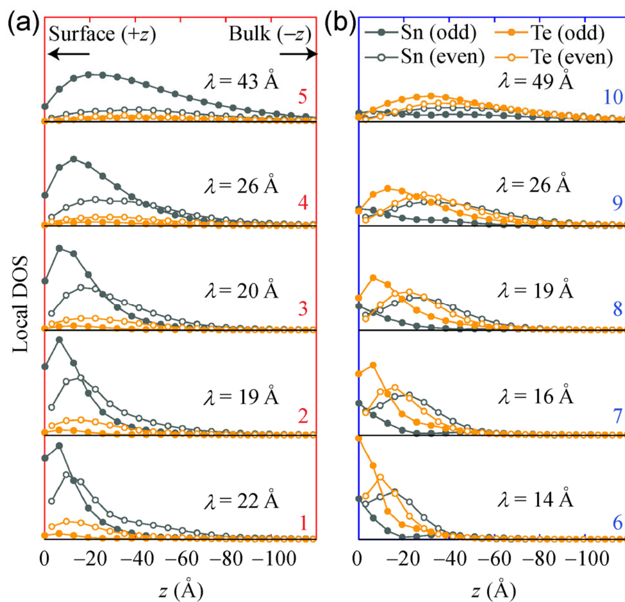

Figure 3 Atom-projected local density of states of 10 selected surface states near the Dirac cone. The corresponding positions of the selected states are marked in the band structure shown in Fig. 2(a). (a) For states 1–5 dominated by Sn, and (b) for states 6–10 dominated by Te. The selected $\boldsymbol{k}$-points are located at 0.617, 0.636, 0.655, 0.675, and 0.694 $Å^{-1}$, and the last $\boldsymbol{k}$-point is also where the zone boundary $\overline{X}$ is. The decay length λ_{nk} is also listed for each surface state. Odd and even here indicate the position of specific atoms. The top surface layer is denoted as Layer 1.

2.3 SnTe nanomembrane

Due to the finite penetration depth of the above isolated surface states, when the thickness of the SnTe membrane decreases to tens of layers, the top and bottom surface states will hybridize with each other, which creates a finite band gap [37]. To demonstrate this hybridization gap and reveal its strain dependence, we built fourteen different slab configurations of SnTe with the number of atomic layers varying from 4 to 49. The slabs sit on the x–y plane as shown in Fig. 4(a) with its unit cell indicated as the blue area containing four atoms. In-plane biaxial strain from –3% to +3% was subsequently applied to each strain-free SnTe membrane of varying thickness, which preserves the mirror symmetry of the SnTe (001) surface with respect to the (110) plane. Geometry optimization leads to the small relaxation of Sn and Te atoms along z shown in Fig. 4(b). We find that Sn atoms near the surface pop out of the x–y plane towards the vacuum while Te atoms contract towards the bulk of the membrane. As illustrated in Fig. 4(c), the first surface BZ (blue square) is simply the projection of the first bulk BZ (purple tetragonal cell) onto the (001) plane. As a result, the high symmetric points (Γ, Z), (X, L), ($\overline{X'}$, $\overline{L'}$) and ($\overline{M}$, A) in the 3D BZ are projected to $\overline{\Gamma}$, $\overline{X}$, $\overline{X'}$, and $\overline{M}$ in the surface 2D BZ.

Figures 4(d) and 4(e) show the strain- and thickness-dependent band structure of SnTe membranes. At a fixed number of SnTe atomic layers, the direct band gap $E_g(\Lambda)$ of nanomembrane increases as the strain increases (note this is opposite to the trend in bulk SnTe, for small tensile strains); while at a fixed strain, the band gap $E_g(\Lambda)$ increases as the thickness reduces due to stronger hybridization effect in thinner membranes. In particular, SnTe nanomembrane with about 40 atomic layers (~12.5 nm) can be tuned from zero gap to a finite gap when the biaxial strain sweeps from –3% to 3%. The tunability of the nanomembrane band gap via elastic strain is significant. For example, the band gap of a 16-layer SnTe nanomembrane increases by more than 50% from 0.1 eV to 0.15 eV under 1% strain. With increasing biaxial strain and decreasing membrane thickness, the band gap varies from 0 to 0.5 eV. The highly tunable band gap, from

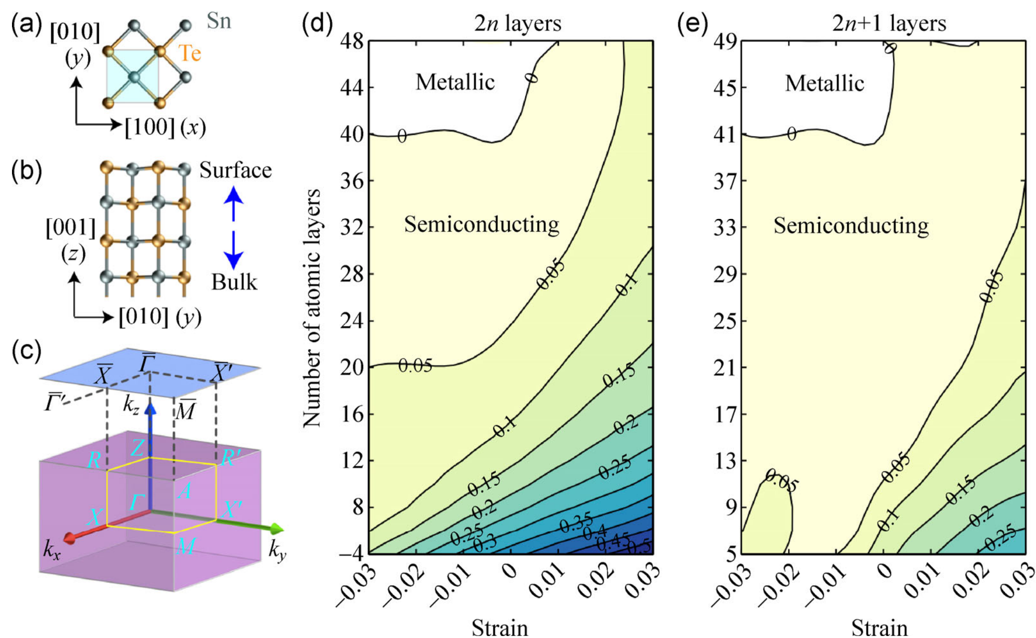

Figure 4 Strain- and thickness-dependent band gaps in SnTe nanomembranes. (a) Top and (b) side view of the equilibrium atomic structure of the SnTe membrane. The shaded area in cyan represents the unit cell for the first-principles calculations. Sn: gray atoms; Te: yellow atoms. (c) Projection of the 3D Brillouin zone (purple) for bulk SnTe onto the 2D surface Brillouin zone (blue) for the SnTe membrane. (d) Biaxial-strain dependent band gap (eV) in membranes with an even number of atomic layers. (e) Biaxial-strain dependent band gap (eV) in membranes with an odd number of atomic layers.

metal to insulator, offers potential applications in thin-film piezoresistive devices, infrared sensors and thermoelectrics.

3 Discussion

3.1 Even–odd oscillation of band gap in SnTe nanomembranes

Comparing Figs. 4(d) and 4(e), there exists a striking behavior in the band gap depending on whether the number of atomic layers in the membrane is odd or even. A better illustration of this even–odd oscillation is shown in Fig. 5(a). This unanticipated behavior of the band gap in fact originates from different inherent symmetry in the slabs with even and odd numbers of layers. In crystalline SnTe (see the unit cell in Fig. 1(c)), there exists a two-fold screw rotation (or glide-reflection) along the [100] (also [010] and [110]) direction with the axis passing through the center of the nearest Sn–Sn bond and a displacement of 1/2 lattice vector in [100] (also [001] and [110]). A screw rotation is incompatible with the Bloch theorem derived from translational invariance of crystals, and thus the two-fold screw rotation naturally introduces double degeneracy for each band at the BZ boundary along [100], i.e., the $\overline{X}$ point (also Z and L). The two-fold screw-rotation-induced double degeneracy is clearly evident in the band structure of crystalline SnTe along Z–R–X in Fig. 5(b). This screw rotation symmetry is preserved in the membrane with an even number of atomic layers, but is broken in the case of an odd number of layers. The degeneracy is, therefore, preserved in the band structure of the even one, while it is lifted in the odd one. The lifted degeneracy in the membrane with an odd number of layers results in a lower CBM and higher VBM at the zone boundary $\overline{X}$ and $\overline{X'}$. Since the band gap of the membrane in the whole 2D BZ is close to $\overline{X}$ and $\overline{X'}$, the band gap in a membrane with an odd number of layers is expected to be smaller than in one with an even number of layers.

To give an illustration, we first establish the ab initio tight-binding Hamiltonian for a SnTe membrane in the bulk quasiatomic Wannier function basis transformed from first-principles Kohn–Sham eigenstates of crystalline SnTe [31–33]. Its unit cell is displayed in Fig. 1(c) and the spin-orbit interaction is included in the first-

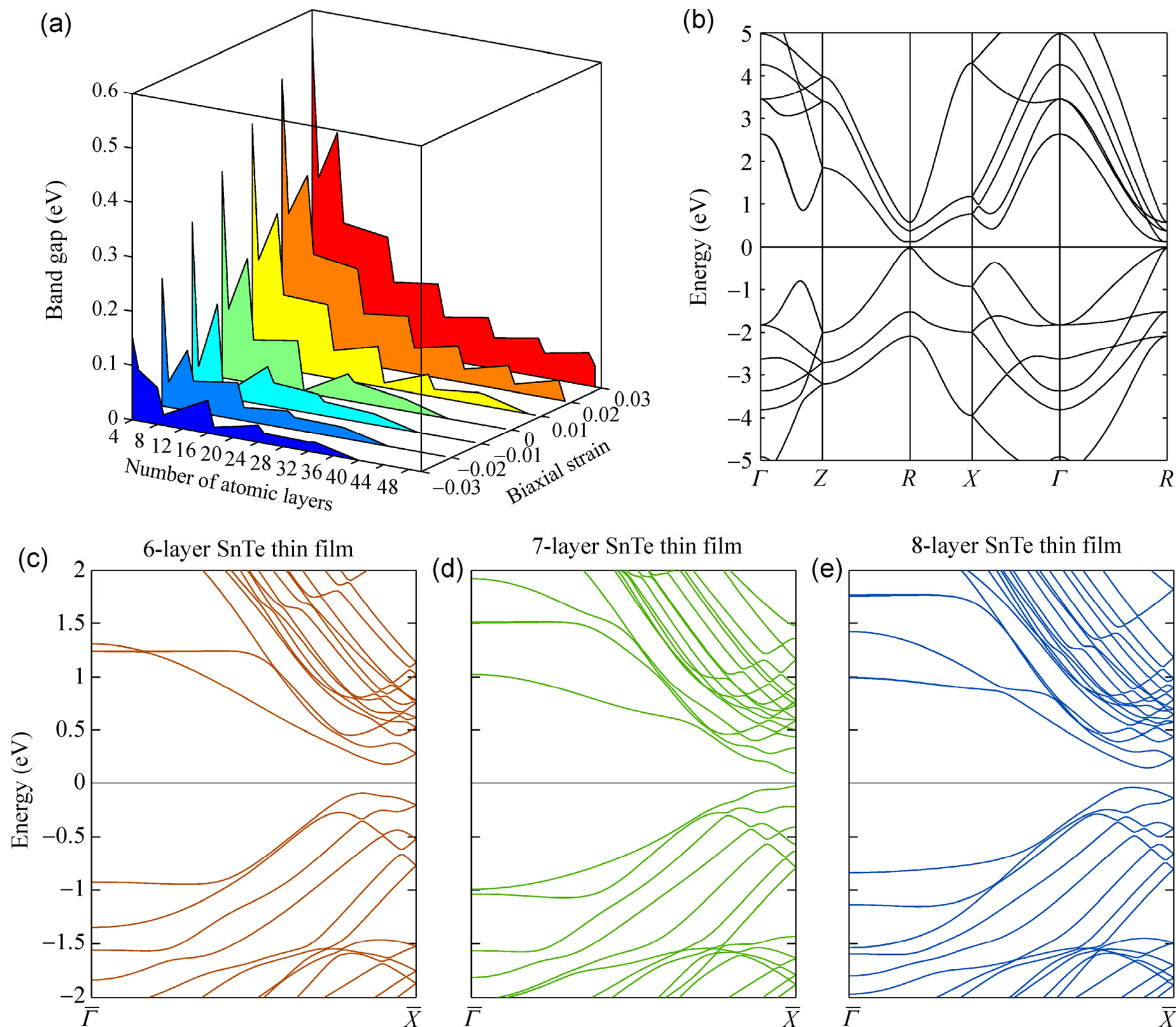

Figure 5 Origin of even–odd oscillation of the band gap in SnTe nanomembranes. (a) Strain- and layer-dependent band gap of SnTe membranes with 14 different numbers of layers, i.e., 4, 5, 8, 9, 16, 17, 24, 25, 32, 33, 40, 41, 48, and 49. (b) Band structure of bulk SnTe with four atoms per unit cell at strain free condition. Its unit cell is shown in Fig. 1(c). Band structure of (c) 6-layer, (d) 7-layer, and (e) 8-layer SnTe nanomembranes. The degeneracy at the zone boundary $\overline{X}$ is preserved in both the 6- and 8-layer cases protected by two-fold screw rotation symmetry, but is broken in the 7-layer case due to the absence of this symmetry.

principles calculations. The calculated electronic band structures of 6-, 7- and 8-layer SnTe slabs along $\overline{\Gamma X}$ are shown in Figs. 5(c)–5(e). At $\overline{X}$, energy bands of both 6- and 8-layer SnTe slabs exhibit a four-fold degeneracy with two-fold spin degeneracy and the other two-fold from the above screw rotation symmetry. However, in the case of 7-layer SnTe slabs the former symmetry is broken while the spin degeneracy is still conserved, and therefore the four energy bands are split into two sets of two-fold degenerate ones. The lifted degeneracy in the 7-layer SnTe slabs also shifts the VBM and CBM to $\overline{X}$, resulting in a direct band gap in contrast to the indirect band gap in the vicinity of $\overline{X}$ in the even layer case.

3.2 Strain-induced electronic phase transition in SnTe nanomembranes

To understand the origin of the above strain-induced band gap change and gap closing/opening, we calculated the first-principles strain-dependent band structure of a 40-layer SnTe membrane displayed in Fig. 6(a). It clearly shows the finite band gap $E_g(\Lambda)$ (a quantity for SnTe nanomembrane) under the biaxial strain of above 1%.

The VBM and CBM states in the nanomembrane close to $\overline{X}$ are presented in Fig. 6(b). A schematic is

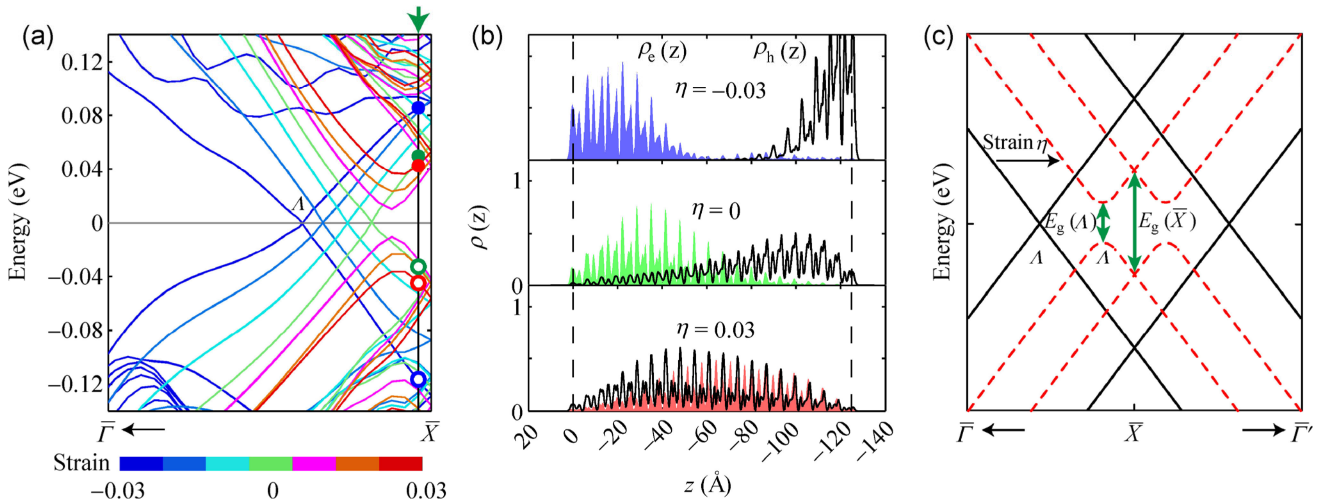

Figure 6 Strain-induced electronic phase transition for a 40-layer SnTe nanomembrane. (a) First-principles electronic band structures of a 40-layer SnTe nanomembrane under biaxial strain from –3% to +3%. (b) Strain-dependent charge density profiles of CBM (shaded area) and VBM (black curves) surface states close to $\overline{X}$, corresponding to the electrons and holes marked as filled and unfilled dots in (a). The charge density profiles are obtained from first-principles calculations and integrated along the *x*–*y* plane parallel to the membrane surface. (c) Schematic of strain-induced electronic band structure change of SnTe nanomembrane.

shown in Fig. 6(c) where the gap is indicated by Λ which is close to the zone boundary $\overline{X}$. As biaxial strain increases, the Dirac cone Λ shifts towards $\overline{X}$ and the band gap $E_g(\Lambda)$ increases. The origin of this can be understood as follows. Biaxial tensile strain causes an increase in the lattice constant, which reduces the band inversion strength in bulk SnTe at $R(L)$ [24]. Because $R(L)$ in bulk BZ is projected onto $\overline{X}$ in the surface BZ (Fig. 1), the band inversion strength in semi-infinite SnTe at $\overline{X}$ also linearly decreases, resulting in a decreasing energy gap between VBM and CBM at $\overline{X}$ in semi-infinite SnTe, labeled as $E_g^S(\overline{X})$. The $E_g(\overline{X})$ of a SnTe nanomembrane approaches $E_g^S(\overline{X})$ when the membrane is thick enough, and both show the same trend with strain, as does $E_g(\Lambda)$: all three quantities decrease with increasing tensile strain. This can be verified by comparing Fig. 2(a) and Fig. 6(a). Since the position of Dirac cone Λ is determined by the intersecting point of the inverted bands [37, 38], the cone of the nanomembrane then moves closer to $\overline{X}$ as $E_g^S(\overline{X})$ and $E_g(\overline{X})$ decrease under increasing strain. As demonstrated in Fig. 3, the penetration length of the surface states strongly depends on the 2D BZ ***k***-point, hence the closer the Dirac point Λ is to $\overline{X}$, the longer is the penetration length. Therefore, under increasing strain, the $E_g(\Lambda)/E_g^S(\overline{X})$-reduction-induced cone shift leads to an increase in the penetration length of surface state in semi-infinite SnTe. This gives rise to an exponential increase in the hybridization strengths of two TCI surface states at opposite sides of SnTe nanomembrane, and thus dramatically increases the hybridization gap $E_g(\Lambda)$ of the nanomembrane. In contrast, compressive strain reduces the surface state penetration length [39]. For thinner SnTe membrane, the finite intrinsic penetration depth λ_0 causes a large hybridization gap even with no strain, and it remains finite under small strain from –3% to 3%. From Fig. 6(a), the estimated average ***k***-shift of the Dirac point Λ along the [100] direction in the 40-layer SnTe is +0.0143 Å^{-1} per 1% biaxial-strain, while the corresponding change of $E_g(\overline{X})$ is about 16 meV per 1% biaxial-strain. The strain-tunable band gap in TCI thin films and its underlying mechanism described above are the main results of our work. The significance and implication of the strain-dependent Dirac cone shift are discussed next.

3.3 Electronic hybridization induced semiconducting surface states in SnTe nanomembranes

The symmetry-protected spin-momentum locking in the surface states can help reduce back scattering in carrier transport, enhance carrier mobility, and thus lower Joule heating. It is particularly useful for designing electronic and spintronic devices with

reduced dissipation. A natural question is: how does the electronic structure change prior to the emergence of massless Dirac cone with increasing membrane thickness? We plot in Fig. 7(a) the energy dispersion of a 16-layer strain-free SnTe membrane which is thin enough to have a finite band gap $E_g(\Lambda)$, yet thick enough to allow us to distinguish top and bottom surface states. Former massless Dirac cones near the Fermi level are now separated by a finite energy gap, forming two massive Dirac cones. Due to double degeneracy, only four surfaces near the Fermi level are distinguishable from the energies in Fig. 7(a). Hence to reveal the spin texture near the massive cones, we separate the double-degenerate surfaces into two groups according to the charge center in the z direction $\langle z_{nk} \rangle$. The band structure and spin texture of the bands with their charge center close to the top and bottom surface are displayed in Figs. 7(b) and 7(c) respectively, with spin texture indicated by arrows and color-coded by $\langle z_{nk} \rangle$. The original chiral texture close to the massless Dirac cones in Fig. 7 cannot be clearly distinguished in Figs. 7(b) and 7(c) as $\langle z_{nk} \rangle$ of the corresponding doubly degenerate eigenstates are very close to each other (near the center of the 16-layer slab). Nonetheless, away from the massive Dirac cones (e.g., towards $\overline{\Gamma}$ and $\overline{\Gamma}'$) the large in-plane spin moments exhibit a similar pattern as Fig. 6, and their charge center $\langle z_{nk} \rangle$ becomes closer and closer to the top and bottom surfaces, which is consistent with the trend in the spatial penetration of surface states at the massless Dirac cone displayed in Fig. 3.

Interestingly, Figs. 7(b) and 7(c) demonstrate the existence of in-plane chiral spin texture at $\overline{X}$ that is similar to the case in Fig. 2. This robust chiral texture at $\overline{X}$ after the membrane thickness reduction is due to the two-fold screw rotation mentioned above. The similar in-plane spin textures around $\overline{X}$ in both massless and massive Dirac cones indicate that the spin-momentum texture happens before the emergence

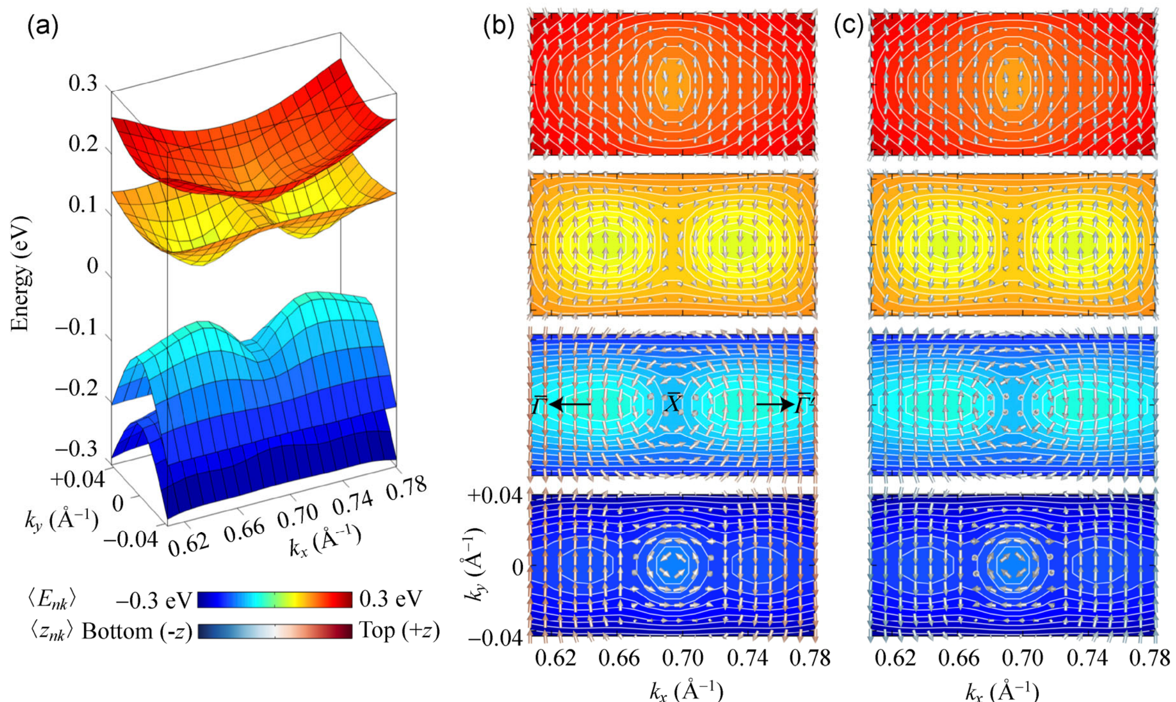

Figure 7 Band structure of a 16-layer SnTe nanomembrane under strain-free conditions. (a) Energy dispersion of eight electronic bands close to the Fermi level in the 2D Brillouin zone around $\overline{X}$. Due to double-degeneracy, only four surfaces are distinguishable in (a). These eight bands are separated into two groups in (b) and (c) according to the charge center position $\langle z_{nk} \rangle$ in the z direction. (b) Energy contours and spin texture of the first group with their charge center position close to the top surface. (c) Energy contours and spin texture of the second group with their charge center position close to the bottom surface. The arrows in (b) and (c) for spin textures are colored according to the charge center position relative to the top and bottom surface.

of the massless Dirac cone, thus the back-scattering of carriers in semiconducting SnTe membranes should also be reduced significantly compared to ordinary semiconductors without spin texture.

4 Applications

The strain-tunable bandgap of SnTe membranes enables us to design a frequency-resolved ultrathin infrared photodetector. A schematic of the setup is shown in Fig. 8. A SnTe nanomembrane with spatially varying width is in contact with two types of electrodes exhibiting different work functions. Because of the inhomogeneous strain induced by the force concentration [40], the optical band gap shows a spatial variation: the narrower the membrane ribbon, the higher elastic strain, and thus the higher band gap. This allows for the detection of multi-energy photons within a single device. The photoexcited electrons and holes will migrate towards cathode and anode, forming a measurable photocurrent from the local region. Depending on specific photon energy of interest, one may choose a suitable material, thickness, geometry, and force.

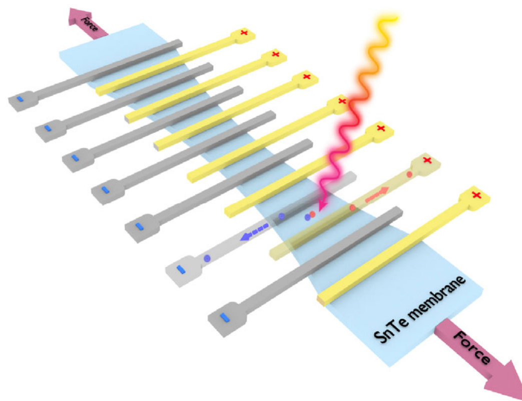

Figure 8 Frequency-resolved infrared photodetector using an inhomogeneously strained SnTe membrane. The spatial variation of the SnTe membrane induces the inhomogeneous strain. The narrower the membrane ribbon, the higher the elastic strain, and thus the higher band gap. Consequently, a spatially dependent optical band gap is achieved. The photoexcited electrons and holes will migrate towards the cathode and anode, forming a measurable photocurrent from the local region. Depending on the specific photon energy of interest, one may choose a suitable material, thickness, geometry, and force.

5 Conclusions

The mechanism of strain-tunable band gap proposed in this work is unique to TCI. For comparison, in Z_2 topological insulators—while the penetration depth of surface states in semi-infinite Z_2 topological insulators can be tuned by strain—the Dirac cone is pinned at time-reversal-invariant momenta, contrary to the strain-induced shift in TCI. On the other hand, while a Dirac cone $\boldsymbol{k}$-shift is known to occur in graphene [41–44], it does not create a band gap as the interior is always gapless. Last but not least, the electronic states in TCI nanomembranes exhibit spin textures, which may be useful for reducing dissipation in applications such as infrared detection and piezoresistive sensing. In addition, elastic strain provides a way to engineer both topologically protected metallic and strong spin-textured semiconducting surface states within a single material. For example, one can elastically stretch the middle part of a SnTe membrane ribbon while leaving the rest stress-free, resulting in a metal–semiconductor–metal pseudoheterostructure within a single SnTe membrane. Inhomogeneous strain-modulated pseudoheterostructures [40, 45] may have applications in novel electronic and optoelectronic devices.

SnTe nanomembranes belong to the class of ultra-strength materials [46, 47], and thus are expected to be able to sustain a large elastic strain before plasticity or fracture takes place. As free-standing ultrathin silicon nanomembranes have been synthesized and demonstrated [48], we expect that ultrathin SnTe membranes can also be synthesized and the elastic strain and membrane thickness controlled metal-to-semiconductor transition in SnTe nanomembranes can be experimentally verified, by for example optical interrogation.

In conclusion, we have demonstrated the possibility of tailoring the electronic band gap and electronic phase transition of a SnTe membrane by varying its thickness and applying elastic strain, and achieved a tunable band gap varying from 0 to 0.5 eV. Our results reveal a striking even–odd oscillation behavior of band gap, the physical origin of which is rooted in the two-fold screw rotation symmetry preserved in

membranes with an even number of layers, which is absent in the case of an odd number of layers. We also found strong spin-textured semiconducting surface states associated with a massive Dirac cone for thin membranes, complementary to topologically protected metallic surface states with a massless Dirac cone for thicker membranes. Membrane thickness control and elastic strain engineering of band gap are generally applicable to other topological insulators. However, elastic strain cannot introduce a Dirac cone shift in Z_2 topological insulator membranes, as the Dirac cone is pinned at time-reversal-invariant momenta. In contrast, strain can introduce a 2D cone shift in TCI surface states even with the protection of crystalline symmetry, making the TCI nanomembrane a unique platform to engineer a pseudo-magnetic field which may directly couple to the spin-texture of the surface states in both metallic and semiconducting states. The present findings will enable the applications of topological (crystalline) insulator nanomembrane in piezoresistive devices, thermoelectrics, and infrared detectors as well as energy-efficient electronic and spintronic devices.

6 Methods

6.1 Atomic and electronic structure of SnTe bulk and nanomembrane

First-principles DFT calculations were performed using the Vienna ab initio simulation package (VASP) [49, 50]. We employed the projector augmented-wave (PAW) method [51], the generalized-gradient approximation (GGA) [52, 53] of exchange-correlation functionals in the Perdew–Berke–Ernzerhof (PBE) form [54], energy cutoffs of 220 eV for plane-wave basis and 380 eV for augmented charge density, and 6 × 6 × 1 Monkhorst–Pack *k*-point sampling [55]. Fourteen slab configurations of SnTe sitting on the *x*–*y* plane were built using the relaxed bulk lattice constant with number of atomic layers varying from 4 to 49. Each configuration was further optimized with maximum energy fluctuation less than 10^{-6} eV, and maximum residual force less than 0.02 eV/Å. In-plane biaxial strain from –3% to +3% was subsequently applied to each strain-free SnTe slab of different thickness. To minimize the periodic image interaction from periodic boundary condition in the calculations, a large vacuum region of more than 20 Å was added along the surface normal. The subsequent electronic band structure for different biaxial strain is obtained from DFT–PBE calculations.

It is worth mentioning that different choices of exchange-correlation functionals may affect the band gaps obtained by DFT calculations, and thus it is desirable that the inverted gap can be verified by several different functionals including hybrid functionals such as HSE. For example, Zhou et al. [56] found that band gaps calculated at the experimental equilibrium lattice constant were 0.173 and 0.094 eV for PBE and HSE hybrid functionals, respectively. Although the PBE band gap is closer to the experimental band gap of 0.18 eV, the slope of the band gap change under biaxial strain may not be very accurate. Nonetheless, the general trend and conclusions of our work should still be valid. Similar studies using hybrid functionals or many-body perturbation theory within the GW approximation [57, 58], though certainly attractive, are beyond the scope of the present work.

6.2 Electronic structure of semi-infinite SnTe

The tight-binding Hamiltonian of a semi-infinite SnTe surface was constructed in the first-principles quasiatomic Wannier function basis [31–33] by knitting a bulk SnTe Hamiltonian and a surface Hamiltonian cut from a fully relaxed 24-layer SnTe slab. An energy shift was introduced to the on-site energy of the bulk Hamiltonian to maintain charge neutrality. The Hamiltonian of a semi-infinite SnTe surface was constructed using a slab of finite thickness with its Hamiltonian component in the coupling region adjusted by a frequency-dependent self-energy correction. The self-energy correction is calculated from a half-surface Green's function using a highly convergent algorithm [34, 35] often adopted in quantum transport calculations [36]. As our main interest is near the mirror-symmetry protected Dirac cone (e.g., within the range of –0.2 to 0.2 eV), we approximate the frequency-dependent self-energy by a constant self-energy matrix calculated at the Fermi level. This approach allows us to directly diagonalize

the self-energy-corrected slab Hamiltonian and extract the surface eigenstates.

Acknowledgements

This work was supported by the National Science Foundation (NSF) DMR-1120901 (X. Q. and J. L.) and U.S. Department of Energy, Office of Basic Energy Sciences, Division of Materials Sciences and Engineering under Award DE-SC0010526 (L. F.). Computational time on the Extreme Science and Engineering Discovery Environment (XSEDE) under grant numbers TG-DMR130038, TG-DMR140003, and TG-PHY140014 is gratefully acknowledged.

References

[1] Hasan, M. Z.; Kane, C. L. Topological insulators. *Rev. Mod. Phys.* **2010**, *82*, 3045–3067.

[2] Qi, X.-L.; Zhang, S.-C. Topological insulators and superconductors. *Rev. Mod. Phys.* **2011**, *83*, 1057–1110.

[3] Xu, S.-Y.; Xia, Y.; Wray, L. A.; Jia, S.; Meier, F.; Dil, J. H.; Osterwalder, J.; Slomski, B.; Bansil, A.; Lin, H.; et al. Topological phase transition and texture inversion in a tunable topological insulator. *Science* **2011**, *332*, 560–564.

[4] Wu, L.; Brahlek, M.; Valdés Aguilar, R.; Stier, A. V.; Morris, C. M.; Lubashevsky, Y.; Bilbro, L. S.; Bansal, N.; Oh, S.; Armitage, N. P. A sudden collapse in the transport lifetime across the topological phase transition in $(Bi_{1-x}In_x)_2Se_3$. *Nat. Phys.* **2013**, *9*, 410–414.

[5] Zhang, Y.; He, K.; Chang, C.-Z.; Song, C.-L.; Wang, L.-L.; Chen, X.; Jia, J.-F.; Fang, Z.; Dai, X.; Shan, W.-Y.; et al. Crossover of the three-dimensional topological insulator Bi_2Se_3 to the two-dimensional limit. *Nat. Phys.* **2010**, *6*, 584–588.

[6] Kim, D.; Cho, S.; Butch, N. P.; Syers, P.; Kirshenbaum, K.; Adam, S.; Paglione, J.; Fuhrer, M. S. Surface conduction of topological Dirac electrons in bulk insulating Bi_2Se_3. *Nat. Phys.* **2012**, *8*, 459–463.

[7] Taskin, A. A.; Sasaki, S.; Segawa, K.; Ando, Y. Manifestation of topological protection in transport properties of epitaxial Bi_2Se_3 thin films. *Phys. Rev. Lett.* **2012**, *109*, 066803.

[8] Xu, S.-Y.; Neupane, M.; Liu, C.; Zhang, D.; Richardella, A.; Andrew Wray, L.; Alidoust, N.; Leandersson, M.; Balasubramanian, T.; Sánchez-Barriga, J.; et al. Hedgehog spin texture and Berry's phase tuning in a magnetic topological insulator. *Nat. Phys.* **2012**, *8*, 616–622.

[9] Checkelsky, J. G.; Ye, J.; Onose, Y.; Iwasa, Y.; Tokura, Y. Dirac-fermion-mediated ferromagnetism in a topological insulator. *Nat. Phys.* **2012**, *8*, 729–733.

[10] Chang, C.-Z.; Zhang, J.; Feng, X.; Shen, J.; Zhang, Z.; Guo, M.; Li, K.; Ou, Y.; Wei, P.; Wang, L.-L.; et al. Experimental observation of the quantum anomalous Hall effect in a magnetic topological insulator. *Science* **2013**, *340*, 167–170.

[11] Wei, P.; Katmis, F.; Assaf, B. A.; Steinberg, H.; Jarillo-Herrero, P.; Heiman, D.; Moodera, J. S. Exchange-coupling-induced symmetry breaking in topological insulators. *Phys. Rev. Lett.* **2013**, *110*, 186807.

[12] Li, J.; Shan, Z.; Ma, E. Elastic strain engineering for unprecedented materials properties. *MRS Bull.* **2014**, *39*, 108–114.

[13] Liu, J.; Xu, Y.; Wu, J.; Gu, B.-L.; Zhang, S. B.; Duan, W. Manipulating topological phase transition by strain. *Acta Cryst.* **2014**, *C70*, 118–122.

[14] Young, S. M.; Chowdhury, S.; Walter, E. J.; Mele, E. J.; Kane, C. L.; Rappe, A. M. Theoretical investigation of the evolution of the topological phase of Bi_2Se_3 under mechanical strain. *Phys. Rev. B* **2011**, *84*, 085106.

[15] Bahramy, M. S.; Yang, B. J.; Arita, R.; Nagaosa, N. Emergence of non-centrosymmetric topological insulating phase in BiTeI under pressure. *Nat. Commun.* **2012**, *3*, 679.

[16] Yang, K.; Setyawan, W.; Wang, S.; Buongiorno Nardelli, M.; Curtarolo, S. A search model for topological insulators with high-throughput robustness descriptors. *Nat. Mater.* **2012**, *11*, 614–619.

[17] Kim, H.-S.; Kim, C. H.; Jeong, H.; Jin, H.; Yu, J. Strain-induced topological insulator phase and effective magnetic interactions in Li_2IrO_3. *Phys. Rev. B* **2013**, *87*, 165117.

[18] Agapito, L. A.; Kioussis, N.; Goddard, W. A., III; Ong, N. P. Novel family of chiral-based topological insulators: Elemental tellurium under strain. *Phys. Rev. Lett.* **2013**, *110*, 176401.

[19] Winterfeld, L.; Agapito, L. A.; Li, J.; Kioussis, N.; Blaha, P.; Chen, Y. P. Strain-induced topological insulator phase transition in HgSe. *Phys. Rev. B* **2013**, *87*, 075143.

[20] Zaheer, S.; Young, S. M.; Cellucci, D.; Teo, J. C. Y.; Kane, C. L.; Mele, E. J.; Rappe, A. M. Spin texture on the Fermi surface of tensile-strained HgTe. *Phys. Rev. B* **2013**, *87*, 045202.

[21] Zhang, Q.; Cheng, Y.; Schwingenschlögl, U. Series of topological phase transitions in $TiTe_2$ under strain. *Phys. Rev. B* **2013**, *88*, 155317.

[22] Qian, X.; Liu, J.; Fu, L.; Li, J. Quantum spin Hall effect and topological field effect transistor in two-dimensional transition metal dichalcogenides. *arXiv:1406.2749*, **2014**.

[23] Fu, L. Topological crystalline insulators. *Phys. Rev. Lett.* **2011**, *106*, 106802.
[24] Hsieh, T. H.; Lin, H.; Liu, J. W.; Duan, W. H.; Bansil, A.; Fu, L. Topological crystalline insulators in the SnTe material class. *Nat. Commun.* **2012**, *3*, 982.
[25] Tanaka, Y.; Ren, Z.; Sato, T.; Nakayama, K.; Souma, S.; Takahashi, T.; Segawa, K.; Ando, Y. Experimental realization of a topological crystalline insulator in SnTe. *Nat. Phys.* **2012**, *8*, 800–803.
[26] Dziawa, P.; Kowalski, B. J.; Dybko, K.; Buczko, R.; Szczerbakow, A.; Szot, M.; Łusakowska, E.; Balasubramanian, T.; Wojek, B. M.; Berntsen, M. H.; et al. Topological crystalline insulator states in $Pb_{1-x}Sn_xSe$. *Nat. Mater.* **2012**, *11*, 1023–1027.
[27] Xu, S.-Y.; Liu, C.; Alidoust, N.; Neupane, M.; Qian, D.; Belopolski, I.; Denlinger, J. D.; Wang, Y. J.; Lin, H.; Wray, L. A.; et al. Observation of a topological crystalline insulator phase and topological phase transition in $Pb_{1-x}Sn_xTe$. *Nat. Commun.* **2012**, *3*, 1192.
[28] Tanaka, Y.; Sato, T.; Nakayama, K.; Souma, S.; Takahashi, T.; Ren, Z.; Novak, M.; Segawa, K.; Ando, Y. Tunability of the ***k***-space location of the Dirac cones in the topological crystalline insulator $Pb_{1-x}Sn_xTe$. *Phys. Rev. B* **2013**, *87*, 155105.
[29] Hohenberg, P.; Kohn, W. Inhomogeneous electron gas. *Phys. Rev.* **1964**, *136*, B864–B871.
[30] Kohn, W.; Sham, L. Self-consistent equations including exchange and correlation effects. *Phys. Rev.* **1965**, *140*, A1133–A1138.
[31] Qian, X.; Li, J.; Qi, L.; Wang, C.-Z.; Chan, T.-L.; Yao, Y.-X.; Ho, K.-M.; Yip, S. Quasiatomic orbitals for *ab initio* tight-binding analysis. *Phys. Rev. B* **2008**, *78*, 245112.
[32] Lu, W. C.; Wang, C. Z.; Chan, T. L.; Ruedenberg, K.; Ho, K. M. Representation of electronic structures in crystals in terms of highly localized quasiatomic minimal basis orbitals. *Phys. Rev. B* **2004,** *70*, 041101.
[33] Marzari, N.; Mostofi, A. A.; Yates, J. R.; Souza, I.; Vanderbilt, D. Maximally localized Wannier functions: Theory and applications. *Rev. Mod. Phys.* **2012**, *84*, 1419–1475.
[34] Lopez Sancho, M. P.; Lopez Sancho, J. M.; Rubio, J. Quick iterative scheme for the calculation of transfer matrices: Application to Mo(100). *J. Phys. F: Met. Phys.* **1984**, *14*, 1205–1215.
[35] Lopez Sancho, M. P.; Lopez Sancho, J. M.; Rubio, J. Highly convergent schemes for calculation of bulk and surface Green-functions. *J. Phys. F: Met. Phys.* **1985**, *15*, 851–858.
[36] Qian, X.; Li, J.; Yip, S. Calculating phase-coherent quantum transport in nanoelectronics with *ab initio* quasiatomic orbital basis set. *Phys. Rev. B* **2010**, *82*, 195442.
[37] Liu, J.; Hsieh, T. H.; Wei, P.; Duan, W.; Moodera, J.; Fu, L. Spin-filtered edge states with an electrically tunable gap in a two-dimensional topological crystalline insulator. *Nat. Mater.* **2013,** *13*, 178–183.
[38] Liu, J.; Duan, W.; Fu, L. Two types of surface states in topological crystalline insulators. *Phys. Rev. B* **2013**, *88*, 241303(R).
[39] Barone, P.; Di Sante, D.; Picozzi, S. Strain engineering of topological properties in lead-salt semiconductors. *Phys. Status Solidi–RRL* **2013**, *7*, 1102–1106.
[40] Feng, J.; Qian, X.; Huang, C. W.; Li, J. Strain-engineered artificial atom as a broad-spectrum solar energy funnel. *Nat. Photonics* **2012**, *6*, 866–872.
[41] Pereira, V. M.; Castro Neto, A. H. Strain engineering of graphene's electronic structure. *Phys. Rev. Lett.* **2009**, *103*, 046801.
[42] Pereira, V. M.; Castro Neto, A. H.; Peres, N. M. R. Tight-binding approach to uniaxial strain in graphene. *Phys. Rev. B* **2009**, *80*, 045401.
[43] Guinea, F.; Katsnelson, M. I.; Geim, A. K. Energy gaps and a zero-field quantum Hall effect in graphene by strain engineering. *Nat. Phys.* **2010,** *6*, 30–33.
[44] Levy, N.; Burke, S. A.; Meaker, K. L.; Panlasigui, M.; Zettl, A.; Guinea, F.; Castro Neto, A. H.; Crommie, M. F. Strain-induced pseudo-magnetic fields greater than 300 tesla in graphene nanobubbles. *Science* **2010**, *329*, 544–547.
[45] Nam, D.; Sukhdeo, D. S.; Kang, J. H.; Petykiewicz, J.; Lee, J. H.; Jung, W. S.; Vučković, J.; Brongersma, M. L.; Saraswat, K. C. Strain-induced pseudoheterostructure nanowires confining carriers at room temperature with nanoscale-tunable band profiles. *Nano Lett.* **2013**, *13*, 3118–3123.
[46] Zhu, T.; Li, J. Ultra-strength materials. *Prog. Mater. Sci.* **2010**, *55*, 710–757.
[47] Zhu, T.; Li, J.; Ogata, S.; Yip, S. Mechanics of ultra-strength materials. *MRS Bull.* **2009**, *34*, 167–172.
[48] Roberts, M. M.; Klein, L. J.; Savage, D. E.; Slinker, K. A.; Friesen, M.; Celler, G.; Eriksson, M. A.; Lagally, M. G. Elastically relaxed free-standing strained-silicon nanomembranes. *Nat. Mater.* **2006,** *5*, 388–393.
[49] Kresse, G.; Furthmüller, J. Efficiency of *ab-initio* total energy calculations for metals and semiconductors using a plane-wave basis set. *Comput. Mater. Sci.* **1996**, *6*, 15–50.
[50] Kresse, G.; Furthmüller, J. Efficient iterative schemes for ab initio total-energy calculations using a plane-wave basis set. *Phys. Rev. B* **1996**, *54*, 11169–11186.
[51] Blöchl, P. E. Projector augmented-wave method. *Phys. Rev. B* **1994**, *50*, 17953–17979.
[52] Becke, A. D. Density-functional exchange-energy approximation with correct asymptotic-behavior. *Phys. Rev. A* **1988**,

38, 3098–3100.

[53] Langreth, D. C.; Mehl, M. J. Beyond the local-density approximation in calculations of ground-state electronic-properties. *Phys. Rev. B* **1983**, *28*, 1809–1834.

[54] Perdew, J. P.; Burke, K.; Ernzerhof, M. Generalized gradient approximation made simple. *Phys. Rev. Lett.* **1996**, *77*, 3865–3868.

[55] Monkhorst, H. J.; Pack, J. D. Special points for Brillouin-zone integrations. *Phys. Rev. B* **1976**, *13*, 5188–5192.

[56] Zhou, D.; Li, Q.; Ma, Y.; Cui, Q.; Chen, C. Pressure-driven enhancement of topological insulating state in tin telluride. *J. Phys. Chem. C* **2013**, *117*, 8437–8442.

[57] Qian, X.; Umari, P.; Marzari, N. Photoelectron properties of DNA and RNA bases from many-body perturbation theory. *Phys. Rev. B* **2011**, *84*, 075103.

[58] Umari, P.; Qian, X.; Marzari, N.; Stenuit, G.; Giacomazzi, L.; Baroni, S. Accelerating GW calculations with optimal polarizability basis. *Phys. Status Solidi B* **2011**, *248*, 527–536.